In-flight Performance and Calibration of the Chandra High Resolution Camera Spectroscopic Readout (HRC-S)[1]

R. P. Kraft, J. H. Chappell, A. T. Kenter, G. R. Meehan, S. S. Murray,
M. V. Zombeck, R. H. Donnelly, J. J. Drake, C. O. Johnson, M. Juda,
D. Patnaude, D. O. Pease, P. W. Ratzlaff, B. J. Wargelin, P. Zhao, G. K. Austin
Harvard/Smithsonian Center for Astrophysics
60 Garden St., MS-31
Cambridge, MA 02138
Phone: 617-496-7709
FAX: 617-496-7700
E-mail: rkraft@cfa.harvard.edu

G. W. Fraser, J. F. Pearson, J. E. Lees, A. N. Brunton
University of Leicester
Leicester LE1 7RH, United Kingdom

M. Barbera, A. Collura, and S. Serio
Osservatorio Astronomico G. S. Vaiana, I-90134 Palermo, Italy

ABSTRACT

The High Resolution Camera (HRC) is one of two focal plane instruments on the NASA Chandra X-ray Observatory (CXO) which was successfully launched on July 23, 1999. The Chandra X-ray Observatory was designed to perform high resolution spectroscopy and imaging in the X-ray band of 0.07 to 10 keV. The HRC instrument consists of two detectors, HRC-I for imaging and HRC-S for spectroscopy. Each HRC detector consists of a thin aluminized polyimide blocking filter, a chevron pair of microchannel plates (MCPs) and a crossed grid charge readout. The HRC-I is an $\sim 100 \times 100$ mm detector optimized for high resolution imaging and timing, the HRC-S is an $\sim 20 \times 300$ mm detector optimized to function as the readout for the Low Energy Transmission Grating (LETG). In this paper we discuss the in-flight performance of the HRC-S, and present preliminary analysis of flight calibration data and compare it with the results of the ground calibration and pre-flight predictions. In particular we will compare ground data and in-flight data on detector background, quantum efficiency, spatial resolution, pulse height resolution, and point spread response function.

[1]Send correspondence to RPK; E-mail: rkraft@cfa.harvard.edu

This paper was published in *X-ray Optics, Instruments, and Missions III*, Joachim E. Truemper and Bernd Aschenbach, Editors, Proceedings of SPIE Vol. 4012, p. 493, and is made available as an electronic reprint with permission of SPIE.

Keywords: X-ray imaging, x-ray spectroscopy, Chandra, AXAF, HRC, High Resolution Camera.

1 INTRODUCTION

The Chandra X-ray Observatory (CXO) was successfully launched from the space shuttle on July 23, 1999, and is providing high spatial resolution imaging (better than 1 arcsecond) and high resolution spectroscopy ($\frac{\lambda}{\Delta\lambda} \sim 1000$ at 1 keV) of cosmic X-ray sources in the 0.07 keV to 10.0 keV bandpass (Weisskopf *et al.* 1995, O'Dell and Weisskopf 1998). The observatory consists of a high resolution X-ray mirror assembly, two sets of transmission grating for dispersive spectroscopy, and two sets of focal plane detectors, the High Resolution Camera and the AXAF CCD Imaging Spectrometer (ACIS). The X-ray mirror assembly (the High Resolution Mirror Assembly or HRMA) is composed of four nested, iridium coated, Wolter type I paraboloid/hyperboloid shells. The Low Energy Transmission Gratings (LETG) are optimized for spectroscopy at the long wavelength end (0.07 to 2 keV or 170 Å to 6 Å) of the CXO bandpass (Brinkman *et al.* 1987). The resolution of the LETG is ~2000 at 170 *Å*. The High Energy Transmission Gratings (HETG) are optimized for dispersive spectroscopy at the shorter wavelength end of the CXO bandpass (0.4 to 10.0 keV or 31 Å to 1.2 Å) (Canizares *et al.* 1987). Each set of focal plane detectors consists of two instruments. The HRC is composed of a wide field, high spatial resolution microchannel plate (MCP) imaging detector (HRC-I), and a long, narrow MCP detector (HRC-S) (Murray *et al.* 1987) that is used to readout the dispersed spectrum from the LETG. The ACIS consists of a 4 CCD imaging detector in a square array which provides imaging and energy dispersive spectra (ACIS-I) and a linear array of 6 CCDs (ACIS-S) that are used to readout the dispersed spectrum from the HETG (Nousek *et al.* 1987).

In this paper, we will discuss the in-flight performance of the HRC-S. In particular, we will present preliminary results from the on-orbit calibration program and compare them with ground calibration results. The main emphasis of this paper is on the quantum efficiency (QE) of the HRC-S and for completeness we present a detailed discussion of the pre-launch calibration of the QE. Other aspects of the in-flight calibration and performance including imaging PSF, background, and UV sensitivity are also discussed. We note that many of the results presented here are preliminary and may be modified as we gain a better understanding of the on-orbit performance of the observatory. This paper is organized as follows. A basic description of the HRC-S is given in section 2. The pre-flight QE calibration is outlined in section 3. In section 4 we describe the on-orbit QE calibration program and present some initial results from the Orbital Activation and Checkout (OAC) phase of the mission. Sections 5, 6, and 7 contain, respectively, discussions and data of the background, UV sensitivity, and imaging performance on-orbit. We end with a brief summary and discussion of future work.

2 INSTRUMENT OVERVIEW

The HRC-S consists of three sets, or segments, of CsI coated MCPs over a continuous hybrid crossed-grid charge detector with an Al/polyimide UV/Ion shield (UVIS). Each segment is composed of a pair of MCPs stacked in a chevron configuration, and is 20 mm×100 mm. The segments are placed lengthwise along the Rowland circle of the LETG with a gap of approximately 4 mm between each segment. The overall length of the HRC-S is ~300 mm. The imaging resolution of the HRC-S is $\sim$ 20 μm (FWHM). The center of the center segment is perpendicular to the optical axis of the telescope, but slightly offset along the +1 order in the dispersion direction so that the gaps between the segments don't occur at exactly the same dispersed wavelengths in the plus and minus orders. The wing segments are slightly tilted relative to the central segment to better match the curved Rowland circle of the LETG for best dispersive wavelength resolution. The detector is covered on five sides by an anti-coincidence shield consisting of a plastic scintillator and photomultiplier tubes to veto charged particle events. A C/Cr coated mirror (the High Energy Suppression Filter or HESF) is also attached to HRC-S. The dispersed spectrum of the LETG can be reflected off this mirror to suppress higher orders in the dispersed spectrum. A schematic view of the HRC is contained in Figure 1. The dispersion relation of the LETG is 1.148

$\AA$/mm; the usable spectral range of the HRC-S extends to $\sim 170\AA$ in the +1 order, and not quite as far in the -1 order because of the offset between the center of the central segment and the optical axis.

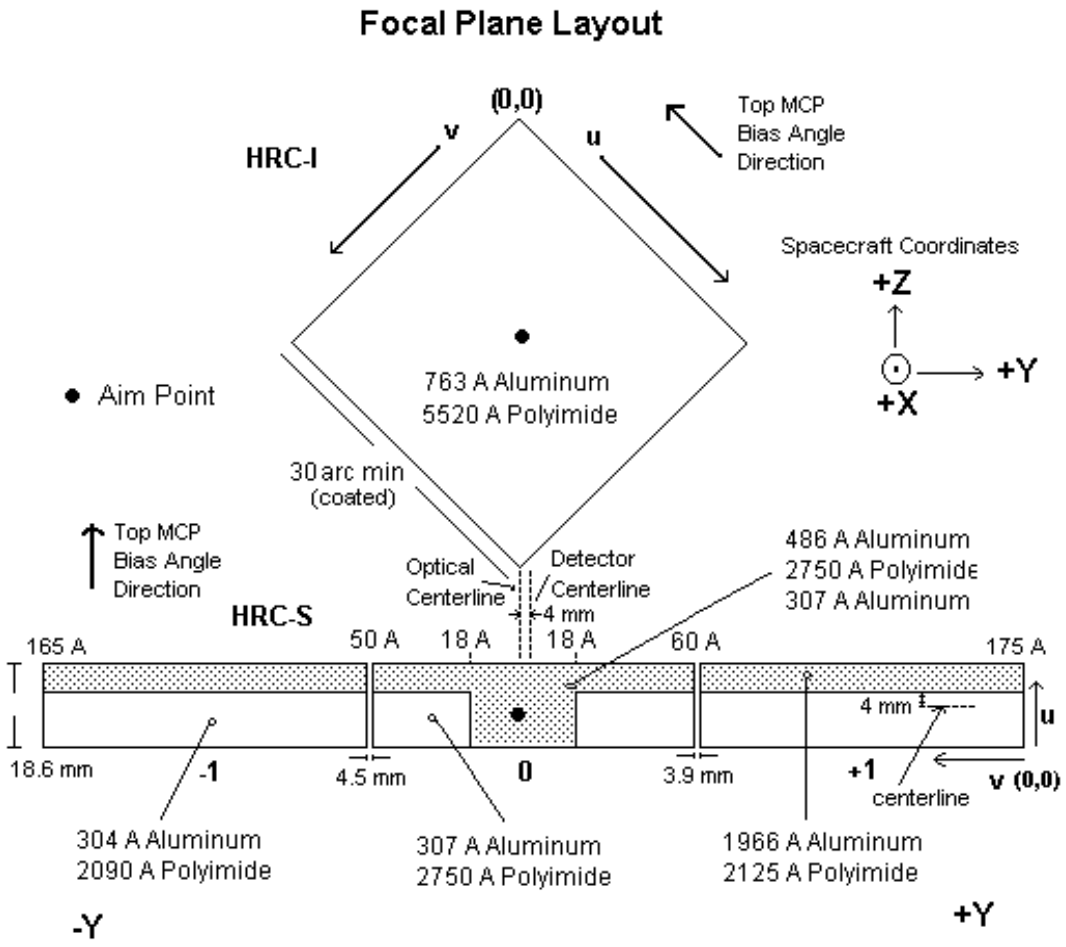

Figure 1: Schematic diagram of HRC UVIS and layout of the instrument.

An Al/polyimide UV/Ion shield (UVIS) is placed $\sim$ 10 mm above each segment to block UV radiation and low energy charged particles. The complex structure of the Al and polyimide of the UVIS was designed to optimize the performance of the HRC-S with the LETG (see Figure 1). The polyimide of the central segment ($2800\AA$) is thicker than that of the wing segments ($2100\AA$) for enhanced UV blocking in the zeroth order of the grating. The central region of the central segment around zeroth order has a thicker region of Al ($800\AA$) than elsewhere for additional UV filtering. This region of thicker Al extends $\sim$31 mm, or to the position where a photon of 18 $\AA$ would be dispersed in first order. Normally the spectrum of the LETG is dispersed along this region of thin Al. In order to estimate the contribution from higher orders, the LETG spectrum can be dispersed along a region of the detector where the Al of the UVIS is considerably thicker ($2000\AA$ on the wing segments). A second function of the UVIS is to provide a well defined electric potential above the surface of the top MCP which improves the imaging performance and to eliminate the time variable background that is often seen on MCP detectors with no shield. A detailed discussion of the UVIS is contained in Meehan *et al.* 1997. A more detailed overview of the HRC-S is contained in Kraft *et al.* 1997.

3 QUANTUM EFFICIENCY

3.1 Pre-flight Quantum Efficiency Measurements

The quantum efficiency (QE) of the HRC-S as a function of energy and position was determined by combining data from three distinct datasets/sets of measurements: the X-ray Calibration Facility (XRCF) HRMA+HRC-S effective area (EA) measurements, flat fields (FF) made in the HRC laboratory at SAO after XRCF, and synchrotron measurements of non-flight CsI coated MCPs around the I and Cs M edges made at the Daresbury Synchrotron Radiation Source. The first two of these were made with the flight instrument, but only the SAO flat fields were made with the instrument in the flight configuration. Electronic modifications were made to the flight instrument after the XRCF measurements (Murray *et al.* 1997, Kraft *et al.* 1997) which significantly changed its performance. An energy (and position) dependent correction factor must be applied to all XRCF QEs to extrapolate them to the current flight configuration. Flat field measurements were taken in both the XRCF and current flight configurations, so that the effect of the electronic changes is calibrated. The third set of data, the synchrotron measurements, were not taken with the flight instrument at all, but with flight-like CsI-coated MCPs. There was no cross-calibration made between the plates taken to the synchrotron and the flight instrument, so there is considerable systematic uncertainty when extrapolating the synchrotron results to the flight instrument. Preliminary discussions of various aspects of the HRC-S ground calibration have been presented elsewhere (Kraft *et al.* 1997, Murray *et al.* 1996, Meehan *et al.* 1997, Kenter *et al.* 1997, Patnaude *et al.* 1998, Kraft *et al.* 1996).

Our general procedure for determining the HRC-S QE as a function of position and energy has been to first determine the MCP QE (i.e. the QE of the flight CsI coated MCPs *without* the UVIS) at normal incidence to the MCP surface as a function of energy in a region around zeroth order at a discrete number of data points. We have used data from the XRCF, which must be corrected for the angle of incidence from the HRMA, and SAO FF measurements. These were all made with the UVIS, so the transmission of the shield must be divided out. The transmission and spatial uniformity of the UVIS have been well calibrated (Meehan *et al.* 1997), so this adds negligible uncertainty. An interpolation algorithm based on the X-ray absorption of CsI is used to extend the HRC-S QE to a finer energy grid between the measurement energies. The synchrotron data around the Cs and I M edges are then incorporated, and the MCP QE is derated by a small factor to correct for the angular dependence of the QE on the HRMA cone angles. This MCP QE is then multiplied by the transmission of the UVIS to determine the HRC-S QE in zeroth order.

There are three additional factors that are considered to determine the spatial and energy dependence of the HRC-S QE. First, based on SAO FF measurements, the average MCP QE of each of the wing segments is $\sim$10% lower than that of the central segment. Second, there is a slight gradient in QE within each segment. The QE increases with increasing V coordinate (i.e. along the dispersion axis) within a given segment. The pattern of QE variation over the entire HRC-S is therefore a sawtooth. The QE variation across a given segment is $\sim$10% and is well described by a linear function. Third, the UVIS has a complex shape that must be taken into account. In this paper we present the MCP QE and HRC-S QE in zeroth order, and the HRC-S QE at the dispersed location of 1st and 3rd orders of the LETG. Each step outlined above is described in more detail below. We have very little pre-flight data on the HRC-S QE below 277 eV, and the limited data that we do have are not self consistent. We have therefore relied entirely on in-flight calibration observations of Sirius B and HZ 43 to provide the calibration at the longest wavelengths (see Section 4).

The effective area (EA) of the HRC-S + HRMA was measured at 57 energies at a position near zeroth order at the XRCF. The details of the experimental setup and measurements at XRCF are contained elsewhere (Kraft *et al.* 1997, Patnaude *et al.* 1998), and will not be repeated here. The HRC-S QE can be determined by dividing out the effective area of the HRMA. We have used the XRCF HRMA model (Zhao *et al.* 1998) of May 1999, and the Mission Support Team (MST) Beam Normalization Detectors (BNDs) (Auerhammer *et al.* 1998) QEs of September 1998. The QE of the instrument changed considerably after the electronic modifications, so a multiplicative correction factor must be applied to all XRCF data to extend it to the flight configuration (see below). In addition, the incident angle dependence of the MCP QE must also be considered when comparing or

combining the XRCF data and the SAO FF data. All XRCF data were taken with the HRMA, while all SAO FF and synchrotron data were taken at normal incidence to the MCP surface. This correction is less than 1% above 400 eV, but can be as large as 20% at lower energies.

Most of the XRCF data were taken using the double crystal monochromator (DCM) or the High Resolution Erect Field Spectrometer (HIREFS) source. A few measurements were made with an electron impact source (EIPS) around zeroth order. In general, the systematic uncertainties associated with the DCM data are small. Higher order contamination is small, and the beam was relatively uniform across the HRMA. We regard the data taken with the DCM as the best available data above 2 keV. They agree to within ~10% with the SAO FF measurements in this bandpass, and this difference provides an estimate of the overall systematic uncertainty of the calibration above 2 keV. Only one EIPS measurement (at 277 eV) is used in this analysis. The HIREFS source was used for EA measurements in the 400 eV to 2000 eV bandpass. There are two complexities of this source that make analysis and interpretation of the data much more difficult than either the DCM or the EIPS. First, this source displayed gross non-uniformities across the HRMA, as much as a factor of 3 in some cases. Second, spectral contamination from tungsten M lines around 1.7 keV as well as higher orders of the nominal calibration energy provide considerable complication given that the HRC has very poor intrinsic energy resolution. The systematic uncertainties associated with data taken using this source are considerably higher than for either the EIPS or DCM. The quality of this data gets progressively worse toward the lower end of the bandpass. We have used the HIREFS data above 1.5 keV in our modeling of the HRC-S QE. Below 1.5 keV, both the statistical and systematic uncertainties become large. We have only used the HIREFS data in this bandpass for qualitative comparison with the absorption model. A complete discussion of the instrumentation used at the XRCF is given elsewhere (Kolodziejczak *et al.* 1995).

3.1.1 SAO Flat Field Quantum Efficiency and Detector Uniformity Measurements

Flat field measurements were made in the HRC laboratory before and after the electronic modifications to measure the HRC-S QE in the flight configuration, the uniformity of the detector, and the effect of the electronic changes on QE. A schematic diagram of the experimental setup is given in Figure 2. The HRC-S was attached to a vacuum pipe by a mechanical snout which ensured that only one segment was illuminated at any time. X-rays were generated by a multi-anode electron impact source. Beam filters were inserted at the source to reduce the flux and remove continuum contamination. The count rate in the instrument was typically ~1200 cts/s. The central segment was calibrated at 8 energies, and each of the wings segments at 4. A summary of the flat field calibrations is contained in Table 1. Measurements were also made of the reflectivity of the HESF by illuminating the flat and blocking the direct beam onto the detector with a mechanical paddle. The Ag L flat field was not used in this analysis because of large non-uniformities in the beam and the complex L series spectrum centered around the Ar K edge of the proportional counter gas.

Two proportional counters (PC) were used for absolute normalization of the beam. A beam normalization detector (BND) could be inserted and withdrawn via a vacuum feedthrough directly between the X-ray source and the HRC. The BND and the HRC were never run simultaneously because of the proximity of the two detectors and a slow gas leak through the thin BND window. A monitor detector (MD) was placed at 90 degrees to the beam to monitor temporal variations. The take-off angle between the electron impact source and either proportional counter was 45 degrees, so the intensity at either detector should be the same, assuming that the beam filters are identical. We do not rely on this assumption, however. Our calibration technique was to simultaneously illuminate the BND and MD to make an absolute measurement of the X-ray intensity and cross-calibrate the two proportional counters. The HRC and MD were then illuminated.

The dead time in the HRC becomes significant at rates above a few hundred cts/s. The HRC electronics are non-paralyzable with an event processing time of 68.5 μs. The true rate, r_t, is given by

$$r_t = \frac{r_m}{1 - \tau r_m}, \tag{1}$$

where r_m is the measured HRC-S rate (cts/s) over the entire detector, and τ is the event processing time. The

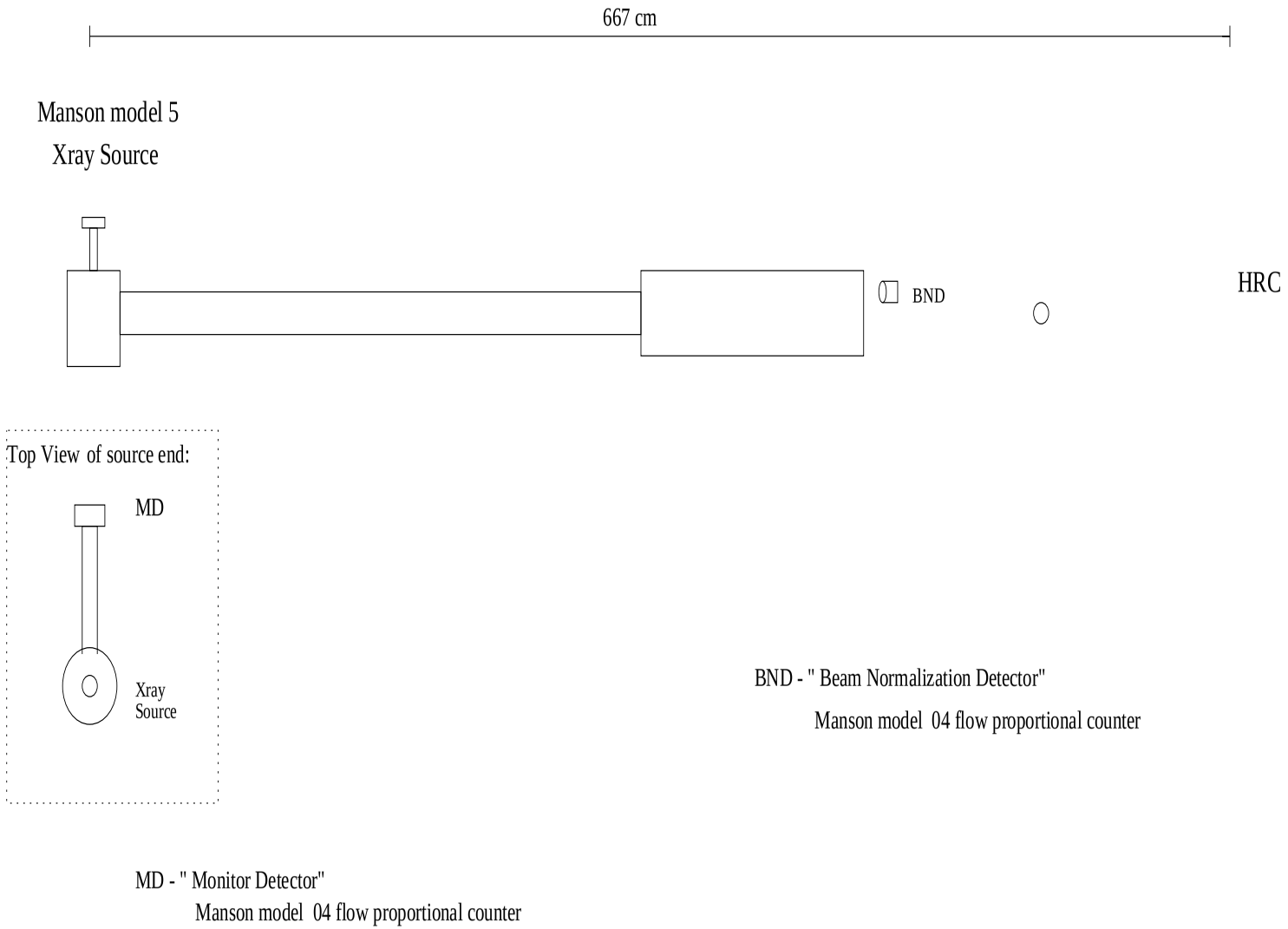

Figure 2: Schematic diagram of experimental setup for HRC flat field measurements.

Line	Energy	Filter	Thickness (MFPs)	V_A	L/C	Seg
B K_α	183 eV	7 μm parylene-C	5.87	600 V	48.4	-1,0,+1
C K_α	277 eV	33 μm polypropylene	5.94	1000 V	171	-1,0,+1
O K_α	525 eV	2 μm Cr	4.67	1000 V	29.3	-1,0,+1
Ni L_α	851 eV	2 μm Cu	3.80	2500 V	2.55	0
Al K_α	1487 eV	50 μm Al	5.40	4000 V	38.9	-1,0,+1
Ag L_α	2984 eV	10 μm Ag	4.86	6000 V	0.60	0
Ti K_α	4511 eV	150 μm Ti	6.80	10000 V	6.73	0
Fe K_α	6404 eV	125 μm Fe	6.97	10000 V	1.78	0

Table 1: Summary of line energies, filters, thicknesses (in mean free paths at the characteristic line), anode voltages, and predicted line-to-continuum ratio (based on theoretical calculations) of the X-ray source for HRC-S flat field measurements.

dead time correction ranges from 2% for the O K_α measurements to 10% for the Al K_α measurements. All flat field QEs have been corrected for dead time.

The measured HRC-S QEs rely on the BND QEs, and any error in the BND QE will translate directly into a systematic error in the measured HRC-S QE. The transmission of the PC windows was measured at a several energies. The thickness of the window was determined by fitting a simple slab absorption model via non-linear regression to this data. The absorption of the PC gas (P-10 or methane) was calculated using the physical depth of the counter, the measured pressure and temperature of the gas, and the 1993 Henke mass absorption coefficients (Henke, Gullikson, and Davis 1993). These counters have not been cross-calibrated against any other detector, nor have they been calibrated in any other manner. Although we rely heavily on this flat field data for our QE calibration, our uncertainties in our overall calibration are not dominated by the systematics at these few flat field energies. As described below, we do not have enough measurements of the QE at enough energies below 1.5 keV. Even if these detectors were now cross-calibrated against, say, one of the MST BNDs or taken to BESSY for a detailed calibration, it would not significantly change the overall uncertainties of the HRC-S ground calibration.

The spectral purity of several of the anodes used in the flat field measurements is relatively low. For the Ti K_α and Fe K_α measurements, there are actually 2 strong lines (K_α and K_β), as well as the bremsstrahlung continuum. A thick filter of the same material as the anode was used to filter out the continuum, but this will have the additional effect of further enhancing the flux in the K_β line relative to the K_α line at the detector. Therefore the assumption of a single monochromatic line is not valid. This problem is most severe for the Ti measurement because the Ti K_α line is on the low energy side of the I L_{III} edge, and the K_β line is above the edge. The MCP QE jumps by approximately a factor of 2 across the edge. The strength of the K_α line relative to the K_β line can be seen in the measured CCD spectrum (Kraft *et al.* 1998) of the Ti anode and Ti filter shown in Figure 3. No sharp HRC spectral features are located between the Fe K_α and K_β line.

We can make a quantitative estimate of the error in the Ti and Fe measurements. Assume that the incident spectrum consists of two spectral lines (i.e. ignore the continuum). The ratio of the flux in the K_β line to K_α line, λ, can be computed from the fluorescent yields of the anode materials and the transmissions of the appropriate filters (Scofield 1974). The calculated ratio is 0.54 for the Ti measurement and 0.57 for the Fe measurement. The CCD spectrum can be used to place a lower limit on this ratio which is consistent with the calculated ratio in both cases. Therefore, under the assumption of monochromaticity, we would make an incorrect estimate of QE at the primary line (the K_α line), Q_1^{MCP}, by a factor f which is given by

$$f = \frac{1 + \lambda \frac{Q_2^{pc}}{Q_1^{pc}}}{1 + \lambda \frac{Q_2^{MCP}}{Q_1^{MCP}}}, \tag{2}$$

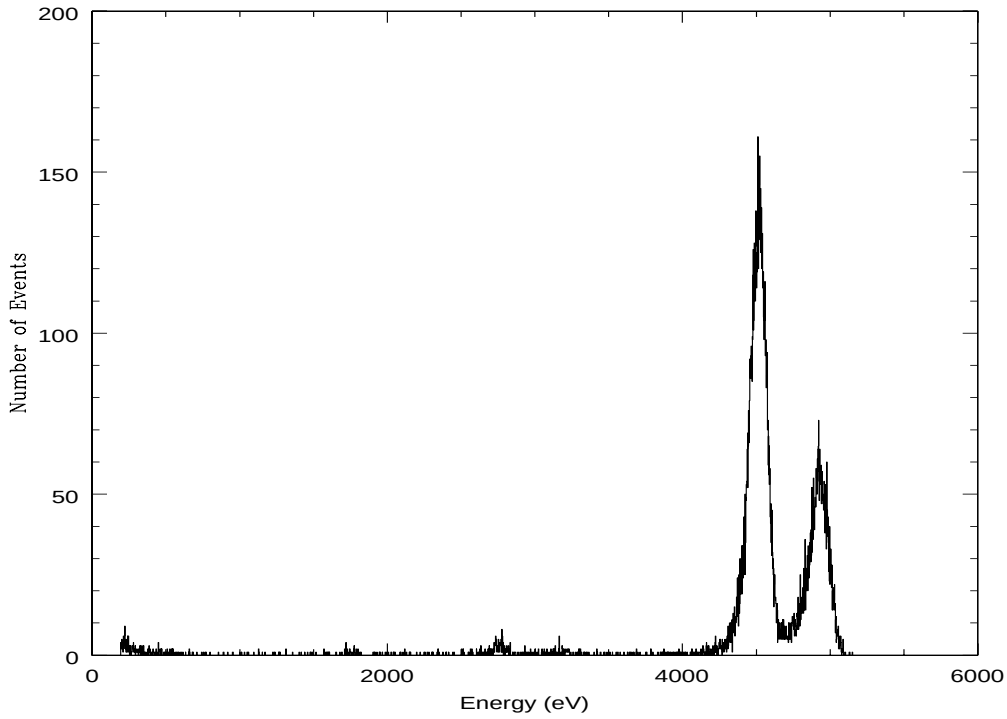

Figure 3: CCD spectrum of X-ray emission from electron impact X-ray source using a Ti anode and 150 Ti μm filter.

where Q_2^{MCP} is the MCP QE at the secondary (K_β) line, Q_1^{pc} is the PC QE at the primary line, and Q_2^{pc} is the PC QE at the secondary line. From the DCM measurements, we have a good estimate of the ratio of the MCP QE at the two lines of interest. By assuming a monochromatic spectrum, we would overestimate the QE at Fe K_α by 4% and by 18.5% at Ti K_α. These corrections have been applied to the data.

The Ni L flat field measurement also has a low line to continuum ratio. The continuum was filtered with a thin Cu foil. This source spectrum consists of the Ni L_α line at 851 eV, a weaker L_ι line at 743 eV, and continuum from ~700 eV to the Cu L_{III} edge at 929 eV and above 1500 eV to 2500 eV (the anode voltage). The error in the QE is not as easy to estimate because of the complexity of the source spectrum, the energy dependence of the PC QE, and the energy dependence of the MCP QE. The MCP QE, in particular, is complex in this spectral region around the Cs and I M edges. For this measurement, there could be a significant (10-15%) systematic error due to this complex source spectrum. Detailed spectral fitting of the PC spectrum or, preferably, the CCD spectrum is required for a quantitative estimate.

As described earlier in this report, the QE of the HRC-S changed significantly when the electronic modifications (Murray *et al.* 1997) were made after XRCF calibration. A plot of the ratio of pre-fix QE to post-fix QE versus energy in a region around the center of the central segment is shown in Figure 4. A cubic spline has been fit to the data points to provide a continuous estimate of the fractional change in QE as a function of energy. The endpoints were chosen arbitrarily to ensure that the spline fit was well behaved at ends of the CXO bandpass. It is necessary to apply this correction to all XRCF EA measurements around zeroth order to adjust them to the flight configuration. Given the large spatial non-uniformities in the pre-fix configuration, the data and curve shown in Figure 4 are not necessarily representative of the change in QE over the entire detector. Most of the spatial non-uniformity present in the detector at XRCF has been removed (see above) however. Note the apparent bump in the spline fit above ~700 eV. This is the region around the Cs and I M edges and it is clear from the pulse height distributions that above about 500 eV, the PHDs become more skewed to higher

pulse heights. The low QE at XRCF was caused by a combination of the low MCP gain and high thresholds, and it is therefore reasonable to expect that if the gain changed in a complex manner with energy after the electronic modifications, the QE could also change in a complex manner, hence the complex shape of this curve.

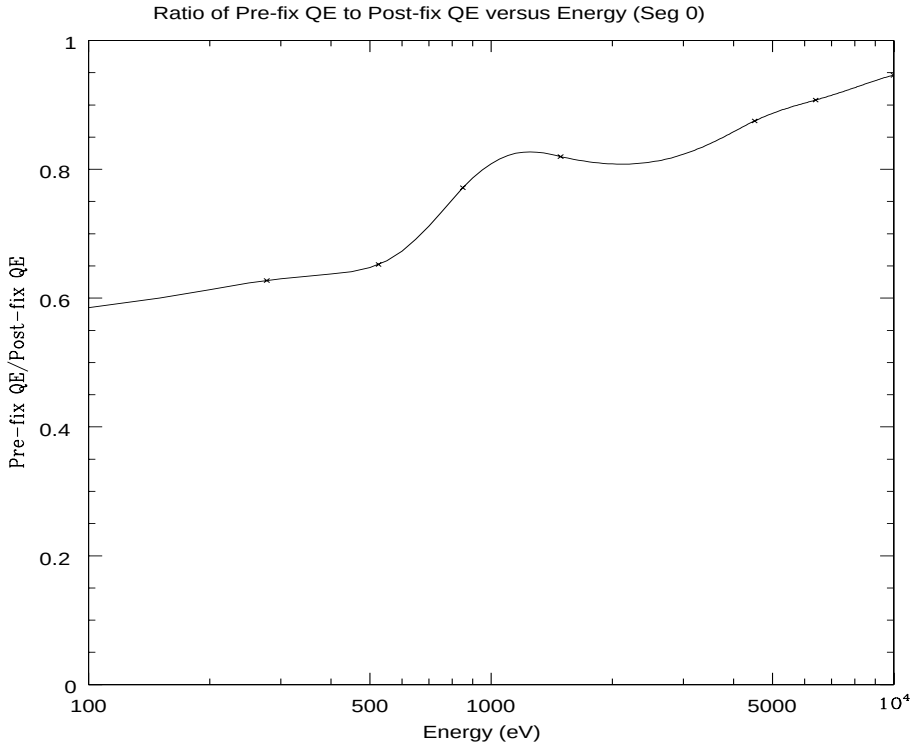

Figure 4: Ratio of pre-fix QE to post-fix QE versus energy in a region around the zeroth order position.

The HRC-S QE measurements made at XRCF and the QE measured in flat fields around zeroth order is plotted in Figure 5 along with statistical error bars. The Xs with error bars are the HIREFS points, the open boxes with the error bars are the DCM points, and the open pentagon with error bars is the EIPS measurements. The open triangles with no error bars are the flat field QE measurements. There are no error bars on these points because the statistical error bars are insignificant compared to the systematic uncertainties. Note the progressively larger error bars at lower energies for the HIREFS data. As described above, we consider only the HIREFS data above 1.5 keV to be reliable for use in the absorption model. We have guided the interpolation so that the derived QE curve in is well behaved regions where we don't have enought reliable data (i.e. between the C K_α and O K_α measurements, and just below the I L_{III} edge).

From 1.5 keV to 10 keV, we have a considerable number of points each with a small (few percent) statistical error. The DCM measurements agree to within $\sim$10% with the SAO FF QE measurements, which is probably a good measure of the systematic uncertainty in this bandpass. Between 277 eV and 1487 keV, however, the only reasonably reliable QE measurements are the 4 SAO FFs and one XRCF EIPS measurement! This is, in our opinion, the major source of uncertainty in the HRC-S QE calibration below 1.5 keV. We do not have QE measurements at enough energies to adequately constrain the shape of the QE versus energy curve. We have synchrotron measurements of the QE between 600 eV and 800 eV that are described in detail below, but this data cannot be combined with the data taken with the flight instrument in a straightforward manner. Below 277 eV, the only data we have are the SAO FF and an XRCF EIPS QE measurement at 183 eV, as well as synchrotron measurements on CsI coated MCPs. These three measurements at the low energy end of the bandpass are not self-consistent, so we will use the inflight observations of Sirius B and HZ43 as the definitive measure of the QE in this range. We regard the pre-launch QE below 0.277 keV as uncalibrated.

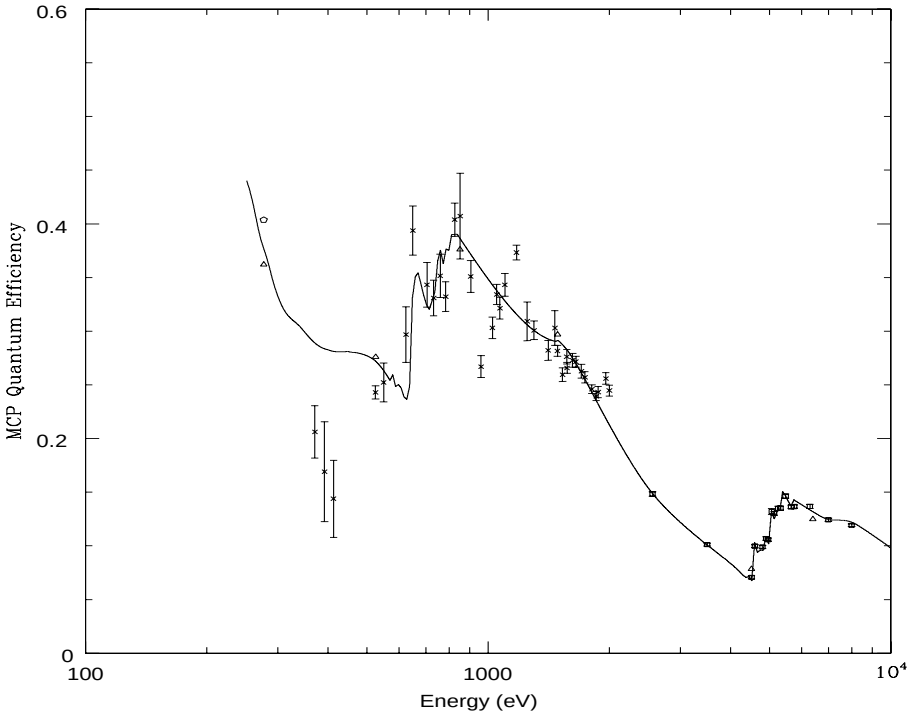

Figure 5: Pre-flight MCP QE of HRC-S in a region around the zeroth order. The Xs with error bars are the HIREFS points, the open boxes with the error bars are the DCM points, and the triangles with error bars are the EIPS measurements. The open triangles with no error bars are the SAO flat field QE measurements.

3.1.2 MCP QE Absorption Model - interpolation to a finer energy scale

A semi-empirical model outlined in a memo by M. Juda (1997) was used to generate the interpolated MCP QE over a finer energy mesh in the 277 eV to 10000 eV bandpass. The model will be summarized here in detail for completeness. It is assumed that the QE of CsI coated MCPs, Q_{MCP}, can be described by a function of the form

$$Q_{MCP} = f(1 - exp(-y(E))), \tag{3}$$

where f is the open area fraction of the MCPs (0.58), and y is the electron yield, that is, the average number of photo-electrons generated by an X-ray of energy E that escape the CsI and are accelerated down the pore to record a detectable event. The MCP QE is therefore given by f times one minus the probability that an event creates no electrons with are detected. We assume that the yield, $y(E)$, is given by

$$y(E) = \Lambda(E)\rho_{CsI}\mu(E)_{CsI}, \tag{4}$$

where $\Lambda(E)$ is an 'electron range' parameter (units of cm), ρ_{CsI} is the mass density of CsI, and $\mu(E)_{CsI}$ is the mass absorption coefficient of CsI. The parameter $\Lambda(E)$ contains all of the complex physics of the initial charge generation and electron transport. It is expected that Λ is a weak function of E, so that the MCP QE is governed primarily by the absorption properties of CsI. There is experimental evidence that this model is a reasonable representation of the response of photocathodes (Henke, Knauer, and Premaratne 1981).

Given the measured QEs, Λ can be found at each energy by inverting Equation 4. A spline curve is fit to the measured Λ at a much finer energy grid, and $Q_{MCP}(E)$ is then computed by inserting the empirically determined $\Lambda(E)$ back into Equation 4. The 1993 Henke mass absorption coefficients for Cs and I are used.

This model provides a reasonable approximation to the data except around the M absorption edges. Based on a comparison with synchrotron measurements, this model overestimates the jump ratio at the M (and L) absorption edges and positions the M edges at the wrong energies. The displacement of the M edges of high-Z materials from previously tabulated values has been seen in reflectivity measurements and is well understood (see, for example, Owens, *et al.*, 1996). Since the jump ratio at the M edges is overestimated, the shape of the curve above the edge is also incorrect.

Synchrotron measurements of the QE of CsI coated MCPs in the 600 eV to 1200 eV bandpass were made in $\sim$0.5 eV energy steps. A complete discussion of the synchrotron measurements is given in Rideout, *et al.*, 1998. Unfortunately, the results of the synchrotron measurements cannot be combined with the XRCF and SAO FF QE data in a straightforward manner because the absolute QE of the synchrotron data is systematically higher than that measured for the flight instrument, and there is no cross-calibration between the two datasets. The reason for this difference is unknown. The absorption model is clearly inadequate around the Cs and I M edges for the reasons discussed above, so it is important to find an improved model in this bandpass. Even though the absolute normalization is different, we believe the synchrotron data is still useful to constrain the shape of the QE curve, at least better than the absorption model. We have chosen to subtract a constant constant from the synchrotron data to make it consistent with the SAO FF data at the O K_α calibration point. While this is clearly an ad-hoc procedure, the resulting QE curve does have the edges at the correct energy and the jump ratios across the edges are smaller than predicted by the interpolation algorithm. There is clearly considerable uncertainty in this procedure, but we believe it provides a more appropriate treatment around the absorption edges. A second order polynomial was used to model the QE between the 851 eV calibration point and the 1487 eV point to better match the structure in this spectral region than the absorption model. We will better constrain the shape of the QE curve with the on-orbit calibrations.

The curve overplotted on the datapoints in Figure 5 is the MCP QE curve (at normal incidence) derived from the combination of the absorption model and the synchrotron data. As can be seen from the Figure, the model *qualitatively* describes the HIREFS data below 1.5 keV which was not used in generating the model. We recognize the inadequacy of the data and model below 1 keV. To address this problem, we are currently making additional measurements of the QE of CsI coated MCPs in the HRC laboratory to further understand the shape of the QE curve below 1 keV. The QE of the HRC-S (i.e. MCP QE times UVIS transmission) in zeroth order is shown in Figure 6. An additional correction was applied to the modeled MCP QE to account for the incident angle of the photons with respect to the MCP pores integrated over HRMA cone angles (Kenter 1998). This correction is larger than 1% only below 400 eV. The effective area of the HRMA + HRC-S on-axis is shown in Figure 7.

It is necessary to consider several additional spatial effects to determine the QE of the HRC-S at the position where a given wavelength and order is dispersed including the normalization between the segments, the QE gradient across each segment, and the complex structure of the UVIS, and the position and width of the gaps between each segment. Based on the SAO FF measurements, the QE of the two wing segments is $\sim$10% lower at all energies than the central segment. We also made flat field measurements of the QE of the wing segments. The results of these measurements are summarized in Table 2. There is also a gradient in QE across each segment. The magnitude of this gradient is $\sim$10% between the maximum value to minimum value for a given segment. A schematic diagram of the UVIS is given in Figure 1. The exact positioning of the various segments, gaps, the UVIS, the center of the central segment, and the optical axis is discussed in shown in Figure 1. The HRC-S QE at the dispersed location the 1st and 3rd orders of the LETG versus energy is shown in Figures 8 and 9, respectively. Complete tables of zeroth order QE and dispersed QE, as well as a variety of other data products are available on the HRC IPI and the CXC Calibration group webpages:

`http://hea-www.harvard.edu/HRC/HomePage.html`

`http://asc.harvard.edu/cal/`

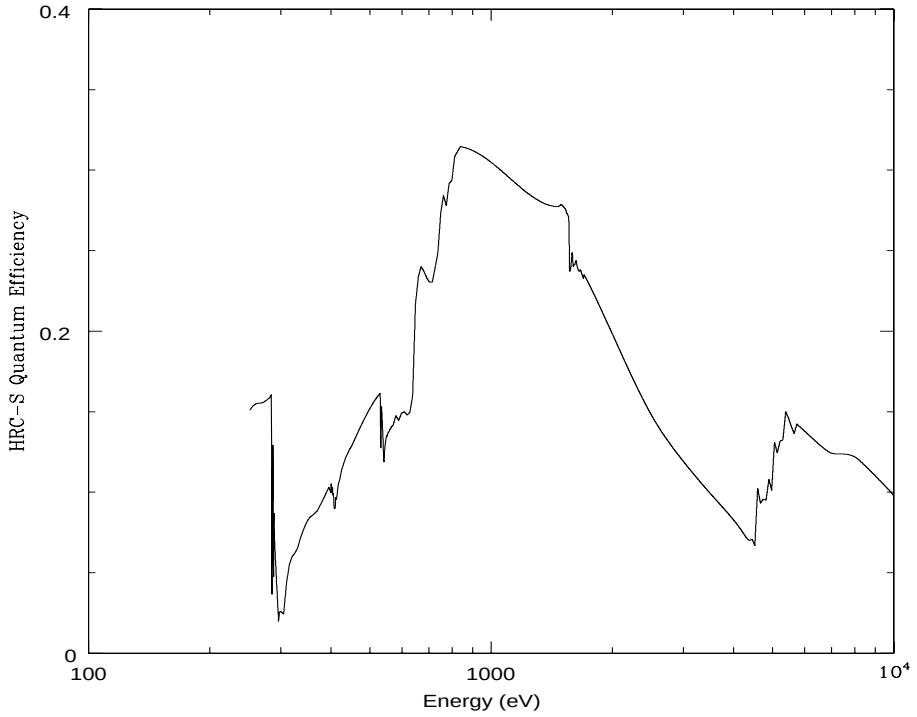

Figure 6: Pre-flight QE of HRC-S (MCP QE and UVIS transmission) versus energy in zeroth order.

Line	Energy	QE (+1 segment)	QE (-1 segment)
C K_α	277 eV	0.230	0.235
O K_α	525 eV	0.187	0.183
Al K_α	1487 eV	0.297	0.295

Table 2: Measured HRC-S QE (UVIS not divided out) for the two wing segments.

3.2 Uncertainty in the Quantum Efficiency Calibration

As described throughout, the major uncertainty in the QE calibration of the HRC-S is the QE of the MCP. Above 1.5 keV, the HRC-S was well calibrated at XRCF, and one can extrapolate this calibration to the current flight configuration. The differences in QE between the XRCF measurements and the SAO FF measurements give a quantitative limit on the systematic uncertainty in the HRC-S QE of ~10%. The systematics of the DCM calibrations are probably better than this. We estimate ~7% uncertainty in the HRC-S QE above 1.5 keV. Below 1.5 keV, however, we just do not have reliable measurements of the QE at enough energies to constrain it to better than ~15% except near the few calibration points. The response of the HRC-S below 200 eV was effectively uncalibrated before launch.

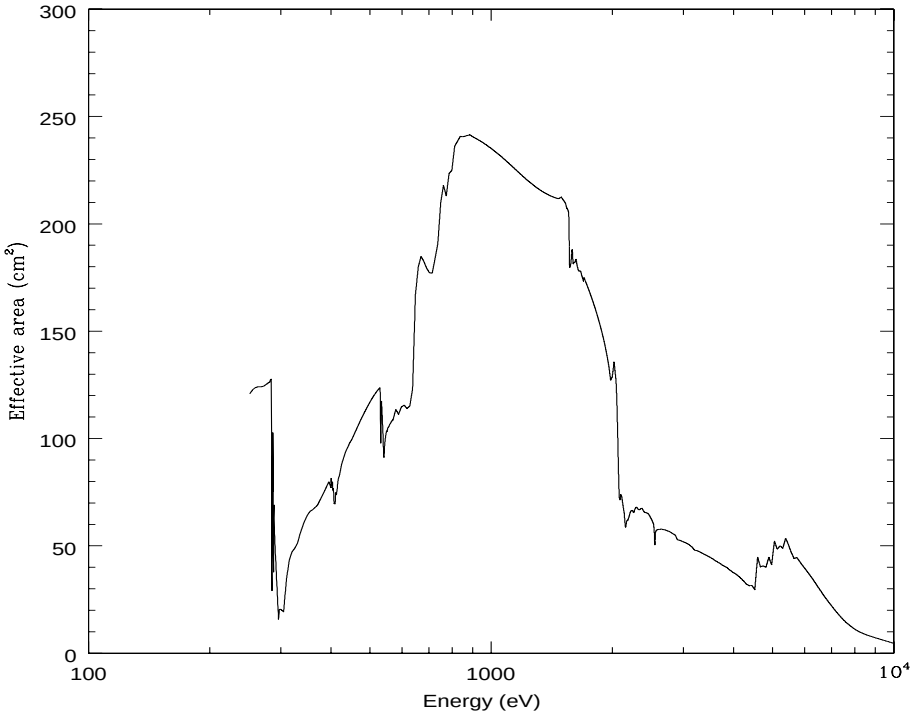

Figure 7: Effective area of HRC-S + HRMA on-axis.

4 IN-FLIGHT PERFORMANCE OF HRC-S

The CXO was launched early in the morning on July 23, 1999. The HRC-S and HRC-S/LETG have undergone extensive testing as part of the Orbital Activation and Checkout (OAC) phase of the mission and are now performing observations as part of routine operations. Preliminary results from an HRC-S/LETG observation of Capella have already been published (Brinkman *et al.* 2000). An HRC-S/LETG spectrum of Capella is shown in Figure 10 that clearly demonstrates the excellent spectral resolution of the HRC-S/LETG. With one exception, the HRC-S and HRC-S/LETG are performing as expected. The background is considerably higher than pre-launch estimates because of a timing problem between the anti-coincidence shield and the event processing electronics. In this section, we will present preliminary results of the analysis of data taken during the OAC phase to verify the detector performance. In particular, we will describe the on-orbit measurements of the HRC-S QE and compare with the pre-launch measurements described above. We will also discuss the on-orbit background, measurements of the UV sensitivity of each segment, and measurements of the imaging performance. A more general discussion of the operational performance of the HRC and a detailed discussion the of LETG are presented elsewhere in these proceedings (Murray *et al.* 2000 and Brinkman *et al.* 2000, respectively).

4.1 In-flight Quantum Efficiency Calibration/Verification

The HRC-S and HRC-S/LETG on-orbit quantum efficiency calibration consists of three types of observations. The first type is a series of HRC-S/HRC-I/ACIS-S imaging/cross-calibration observations of the supernova remnants Cas A and G21.5-0.9. The spectrum from these sources is determined by the ACIS observations; the integrated rate in the HRC provides a measurement of the average QE weighted by the source spectrum.

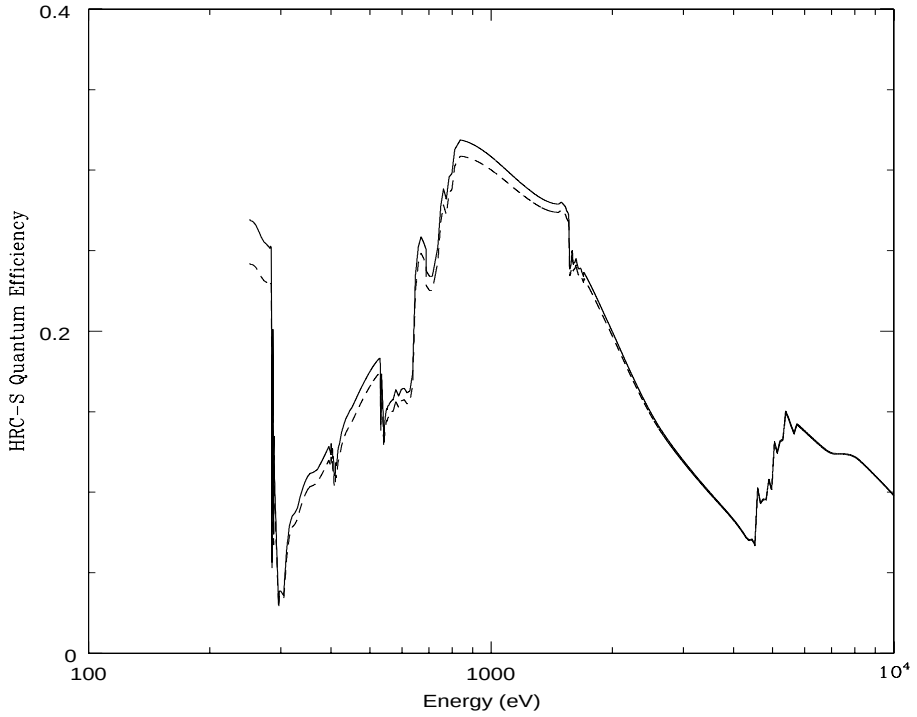

Figure 8: Pre-flight QE of HRC-S (MCP QE and UVIS transmission) in 1st order of the LETG (i.e. QE of the HRC-S at the position where the first order at energy E is dispersed by the LETG) versus energy. The solid curve is the -1 order, the dashed curve is the +1 order.

The second type of calibration observations is HRC-S/LETG observations of the white dwarfs Sirius B and HZ 43. These observations are used as standard candles to determine the long wavelength response of the HRC-S/LETG combination as the EUV/soft X-ray flux from these sources is reasonably well know. The third type of observations are ACIS-S/LETG and HRC-S/LETG cross-calibrations of Capella, a line dominated source, and 3C273, a continuum source which extends to 10 keV. We will present some preliminary analyses from each of these calibration observations.

4.1.1 Broadband Quantum Efficiency Calibration

The supernova remnants Cas A and G21.5-0.9 were observed by the HRC-I, HRC-S, and ACIS-S instruments to cross-calibrate the broadband QE above ~0.8 keV. Each segment of the HRC-S was illuminated by both sources, but unfortunately the observations on the +1 segment were slightly misaligned and a significant fraction of the flux fell in the gap between the +1 and central segments. Analysis of that data would require a detailed exposure correction and is not considered here. As described elsewhere in these proceedings (Kenter *et al.* 2000), the measured rate in the HRC-I agrees within ~10% for both sources with the flux measured by ACIS-S. Given that agreement, we have compared the broadband fluxes for the HRC-S observations of the central and -1 segments with the HRC-I observations. The results are summarized in Table 3. The observation on the -1 segment is approximately 20 arcminutes off-axis so a substantial correction must be applied to that data to account for telescope vignetting. Background was estimated in a region near the source. The estimated rate based on the pre-flight quantum efficiency and ACIS-S spectrum is also given. As described above the pre-flight QE of the HRC-S is somewhat lower than that of the HRC-I, and as can be seen from Table 3, the in-flight calibration is roughly consistent with these pre-flight measurements. For example, we predict a rate of 0.406 cts/s in the

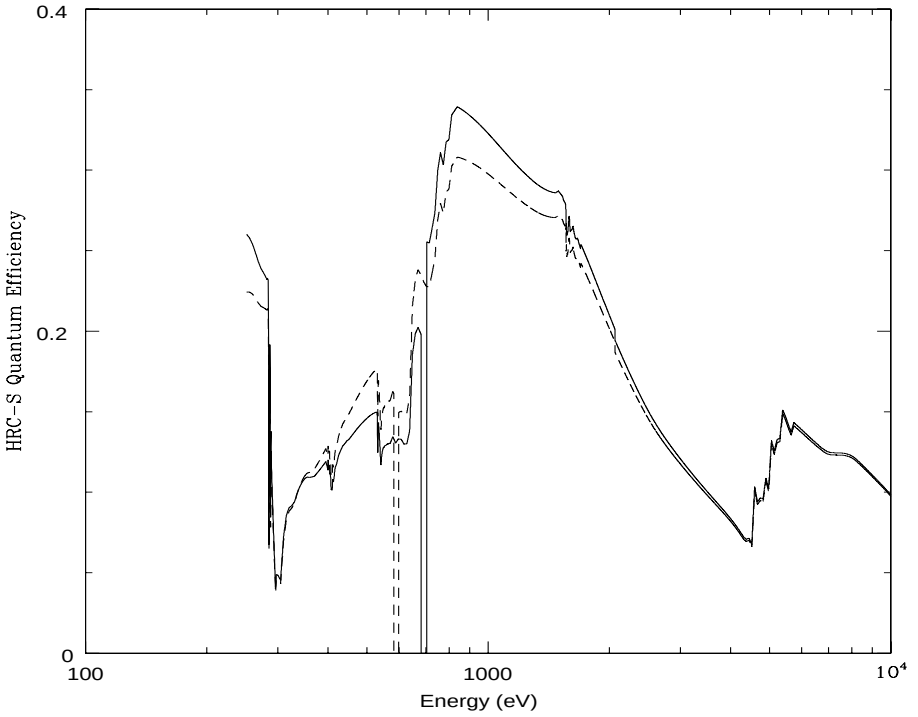

Figure 9: Pre-flight QE of HRC-S (MCP QE and UVIS transmission) in 3rd order of the LETG (i.e. QE of the HRC-S at the position where the third order at energy E is dispersed by the LETG) versus energy. The solid curve is the -3 order, the dashed curve is the +3 order. The dropouts at 700 eV and 600 eV are caused by the gaps between the segments.

central segment based on the ACIS-S observation, and measure a rate of 0.39 cts/s. The G21.5-0.9 observation gives very good agreement in the broadband QE between both segments of the HRC-S and the HRC-I, but the spectrum is well described by an absorbed powerlaw, and the spatial morphology of the remnant is reasonably simple. There is a somewhat larger difference ($\sim$10%) between predicted and measured QEs for Cas A; the predicted rate in the center segment is 78.8 cts/s and the measured rate is 71.9 cts/s. This object has a complex spatial morphology and a line dominated spectrum that ACIS cannot fully resolve, and a more detailed analysis than that given here including the effects of telescope vignetting, spatial variations in the detector efficiencies, and spectral variations in the source may improve the agreement. We therefore conclude that the average, broadband QE above $\sim$0.8 keV is consistent with our pre-flight estimates based on ground calibration data.

Source	HRC-I rate (cts/s)	HRC-S seg 0	HRC-S seg -1	HRC-S pred.
Cas A	82.1	71.9	39.4 (73.9)	78.8
G21.5-0.9	0.56	0.39	0.21 (0.40)	0.406

Table 3: Summary of HRC-S/HRC-I broadband QE cross-calibration observations. The entries in the table are the measured counting rates (cts/s). The HRC-S predicted rate is the rate estimated using the pre-flight quantum efficiency model and the observed ACIS-S spectrum. The rate in parenthesis in the -1 segment column is the rate after correction for the telescope vignetting ($\sim$0.53). The observations with the -1 segment were 20 arcminutes off axis.

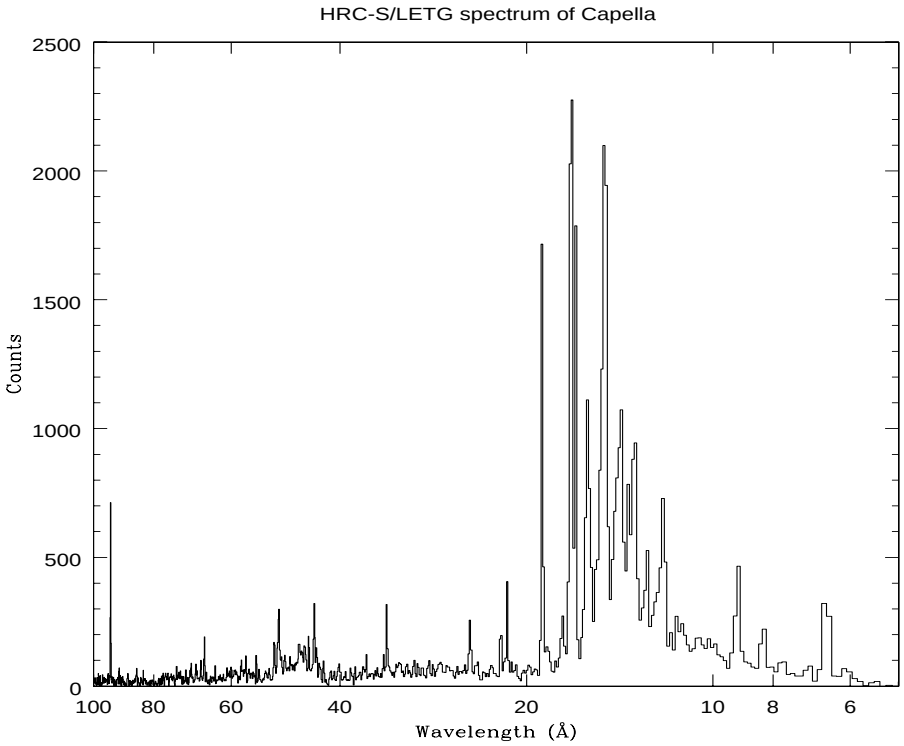

Figure 10: Dispersed spectrum of HRC-S/LETG observation of Capella. The histogram is sum of the number of counts in the positive and negative orders versus wavelength. The data is binned at approximately twice the dispersive resolving power of the LETG.

4.1.2 Low Energy Quantum Efficiency Calibration

Two nearby white dwarfs, HZ 43 and Sirius B, were observed in order to calibrate the long wavelength response of the HRC-S/LETG. As described above, the HRC-S was essentially uncalibrated in this bandpass, so we are relying on this in-flight data to provide the calibration. The usable flux from HZ 43 covers the bandpass 170 Å to 40 Å, and that from Sirius B the bandpass 170 Å to 60 Å. ACIS has no sensitivity in this bandpass, so we must rely on previous observations and models of the absolute flux and spectrum of these objects for an absolute calibration. These observations will therefore define the long wavelength response of the HRC-S. Model spectra for both objects based on EUVE observations were provided to the CXC by Martin Barstow (Barstow, Holberg, and Koester 1995, Paerels, Bleeker, Brinkman, and Heise 1988).

Sirius B was observed three times with the HRC-S/LETG for a total observation time of 48569 seconds. The high background saturated the telemetry (see discussion of the background below), so that a significant dead time correction had to be applied. Using pre-flight models of the HRMA effective area and the LETG dispersion efficiency in first order, the HRC-S QE can be derived using the model spectrum. A plot of the derived QE (average of +1 and -1 order) versus energy is shown in Figure 11. Little systematic error is introduced by using the pre-flight models of the HRMA effective area and LETG efficiency as they are well known from ground calibration measurements and are weak functions of energy in this bandpass. Overplotted on Figure 11 are estimates of the long wavelength response based on ground calibration measurements of the transmission of the UVIS and synchrotron measurements made at the Daresbury Synchrotron Radiation Source of flight-like CsI-coated MCPs (Pearce *et al.* 1995) for purposes of comparison. The synchrotron measurements were not made with the flight detectors, so transferabilitily of the calibration is uncertain, particularly at these energies where details of coating process, handling, and life history can all significantly affect the QE. The large

undulations which are apparent in the pre-flight QE curves are due to the complex absorption of the UVIS. These undulations can also clearly be seen in the Sirius B data giving us confidence that the UVIS data and the Daresbury synchrotron measurements describe shape of the QE curve reasonably well, although the absolute normalization of the synchrotron data is considerably (60%) different.

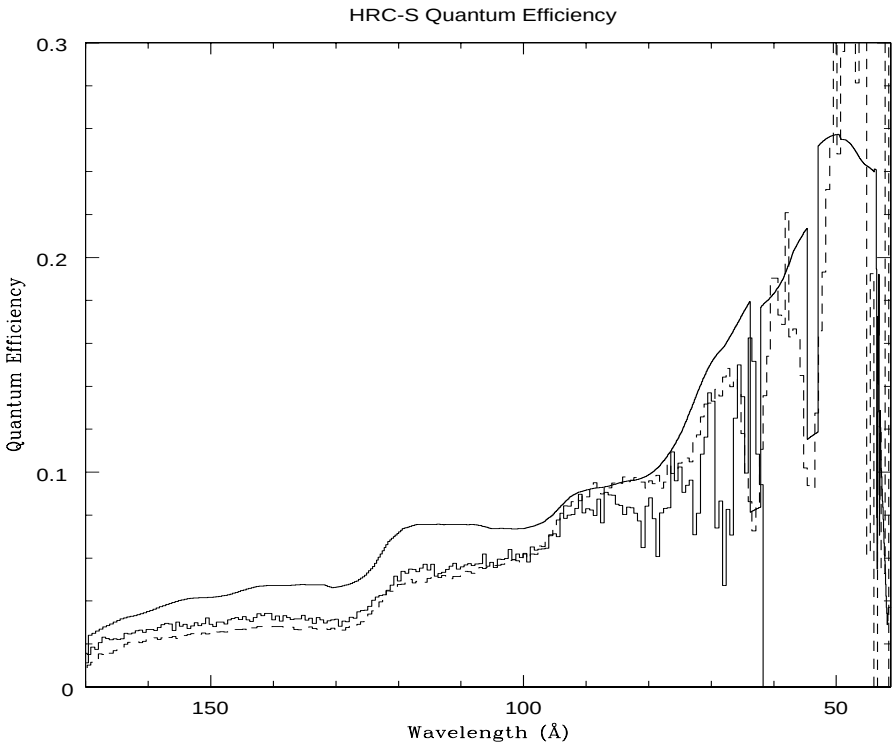

Figure 11: Quantum efficiency of HRC-S/LETG (1st order) based on the observations of Sirius B and HZ43. The solid histogram is the measured QE of the HRC-S averaged over the +1 and -1 orders for Sirius B, and the dashed histogram for the HZ43 observation. The Sirius B data is not shown shortward of 60 Å because the flux is low and the statistical noise large. The continuous curve above the histograms is the average QE in the +1 and -1 orders based on pre-flight measurements of the transmission of the UVIS and synchrotron measurements of flight-like CsI-coated MCPs.

We have also plotted the HRC-S QE derived from a 40358 second observation of HZ 43 in Figure 11. The flux from HZ43 extends to shorter wavelengths than Sirius B, but there is more uncertainty in the fundamental parameters of the stellar atmosphere and hence the spectrum, particularly at the shorter wavelengths. We have therefore chosen the spectrum from a range of spectra whose derived long wavelength QE most closely matches that from the Sirius B observation. The shape of the HZ43 and Sirius B curves (i.e. the undulations due to the UVIS are clearly seen), and the gaps between the segments can also be seen in the proper position. The detector gaps in the spectrum are not sharp, well defined features because the dither slowly moves the position of the gaps in wavelength space relative to zeroth order.

The ratio of the flux in the -1 order to that in the +1 order for the HZ43 observation is used to measure the relative QE of the two wing segments, and is plotted in Figure 12. The predicted pre-flight ratio of the QE of the -1 and +1 orders is also plotted. As described above, there is a ~10% spatial variation in the QE across each segment along the dispersion axis of the LETG. In addition, ground calibration measurements showed that the average QE of the wing plates was about 10% lower than that of the center segment. From 100 eV to 250 eV, the measured ratio of the QEs in the -1 to +1 orders agrees with the pre-flight predictions to within 10%. Below 100 eV, however, the divergence becomes larger. The QE of the +1 segment below 100 eV becomes

decreasingly smaller with decreasing energy compared with the -1 segment.

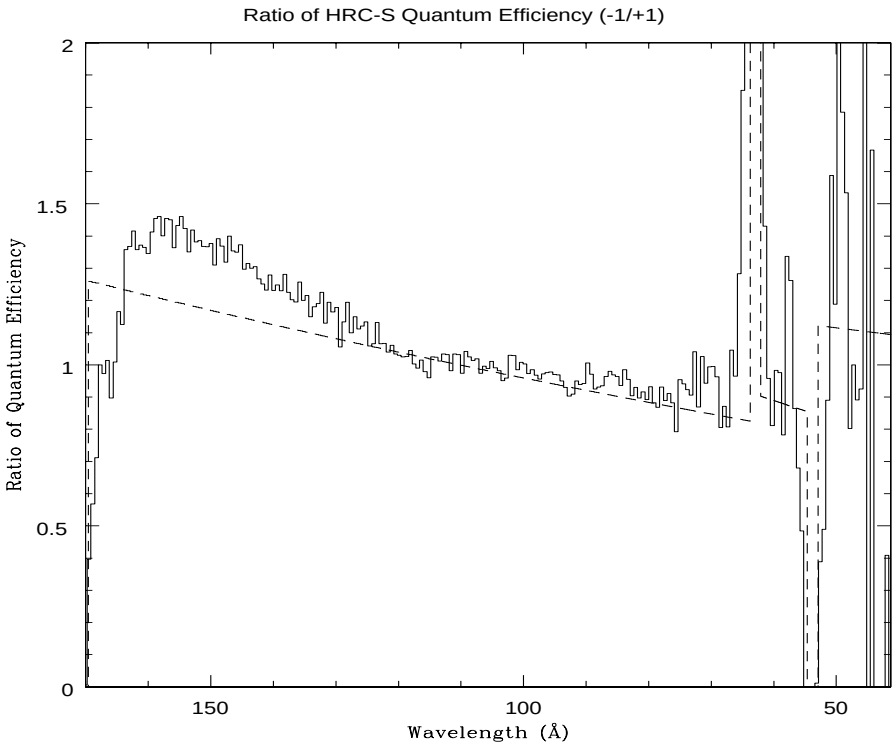

Figure 12: Measured (HZ 43 observation) and predicted ratio (-1/+1) of HRC-S QE at the position where the -1 and +1 orders are dispersed. The histogram is the HZ43 data, and the dashed line is the prediction based on the preflight ground calibration.

4.1.3 HRC-S/LETG and ACIS-S/LETG Cross-Calibration Observation of 3C273

The nucleus of the bright active galaxy 3C273 was observed with the HRC-S/LETG and ACIS-S/LETG (and with the ACIS-S/HETG as well) to cross-calibrate the response of the two detectors with the LETG. This object was chosen because it is a bright, approximately pointlike, source which has not historically exhibited large scale spectral variability on the time scales of hours or days. Only 1300 seconds separate the end of one observation (HRC-S/LETG) and the beginning of the other (ACIS-S/LETG). We present preliminary results of this cross-calibration, but analysis of this data is ongoing. This source was observed for 40298 seconds by HRC-S/LETG and for 39626 seconds by ACIS-S/LETG. We have assumed there was no spectral variation in the source during the observations.

We have made an measurement of the HRC-S QE as a function of energy by using the ACIS-S/LETG observation as an absolute measure of the spectrum of 3C273. The first order ACIS spectrum was extracted using the *tgextract* program of the CXC's Chandra Interactive Analysis of Observations software package. A model of the efficiency of the ACIS-S/LETG combination was created using the preflight calibration measurements so that the absolute flux could be computed from the observed spectrum. The QE of the HRC-S as a function of energy was then computed using this model of the absolute flux. A plot of the derived HRC-S QE is shown in Figure 13. The third order contribution in the HRC-S spectrum was estimated by an iterative technique, and is a significant (10-20%) correction below 1 keV. The error bars on the points only reflect the statistical errors of the HRC-S data. Statistical uncertainties from the ACIS-S data have not been propagated, although they are of the same magnitude or smaller than the HRC-S error bars, and no additional contribution has been added for

any systematic effects. The pre-launch estimates of the HRC-S QE are also shown. Any systematic uncertainties in the LETG and HRMA response will apply equally to both the ACIS-S and the HRC-S observations and will cancel out. Any uncertainties in the QE of the ACIS instrument will, however, directly affect the derived QE. The large jump at around 0.6 keV is due to the dither moving the transition region of the thick/thin Al on the UVIS relative to the dispersed spectrum. A detailed exposure map that accounts for the converging cones of the HRMA beam and for the motion of the position of the zeroth order because of the dither must be created to remove this feature. The dip at 1.8 keV is due to the fact that one order of the ACIS spectrum falls in the gap between chips and has not been properly exposure corrected.

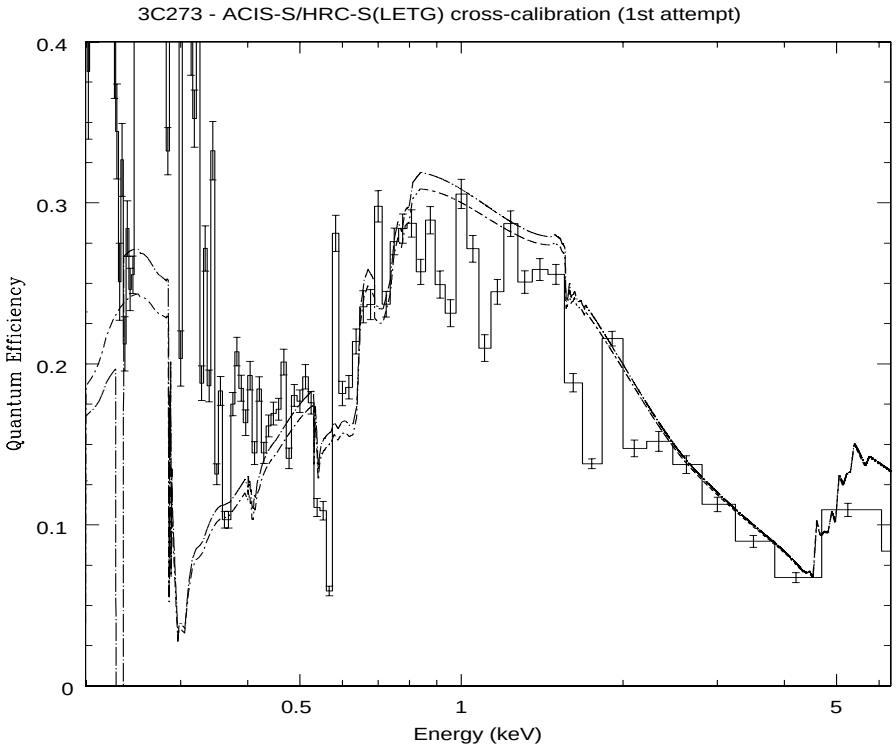

Figure 13: HRC-S/LETG and ACIS-S/LETG cross-calibration of the HRC-S. The histogram with error bars is the QE of the HRC-S at the dispersed location of the first order of the LETG. The error bars only reflect the statistical errors for the HRC-S data. The statistical errors on the ACIS-S data were not propagated, but are somewhat smaller. The two continuous curves are the pre-launch predictions of the HRC-S QE in the -1 (top curve) and +1 orders. We should emphasize that this result relies entirely on the the pre-flight calibration of the ACIS-S.

There is general agreement, within 10-15%, between this observation and our pre-launch model above 0.5 keV. There is considerably divergence between the model and the data below 0.5 keV, however, and below the C K edge, the difference is a factor of 2. It is not possible that the HRC-S QE is twice as high as our pre-launch prediction as that would make the MCP QE considerably greater than the open area fraction of the MCPs. There must be a considerable systematic uncertainty in this energy range. Above 0.4 keV, the QE derived in this measurement is $\sim$10-15% lower than our pre-launch estimates. We hope to improve this result as we better understand the systematics of the data. We have also measured the ratio of flux in the -1 order to the +1 order to confirm the QE gradient on the center segment, but we are currently dominated by systematic uncertainties. A detailed comparison will be described in a future paper.

5 BACKGROUND AND PULSE-HEIGHT FILTERING

The background in the HRC-S is considerably higher than pre-flight predictions because of a timing problem between the anti-coincidence shield and the event processing electronics. The rate over the entire detector is typically 200-250 cts/s. The maximum rate allowed by the telemetry is 184 cts/s, so this high background rate creates significant dead time in all observations. To ameliorate this problem, the detector edge blank feature has been enabled and only events from a region 9.6 mm wide along the full length of the detector are typically processed by the electronics and telemetered to the ground. The quiescent background rate in this reduced region is approximately 85 cts/s, well below the telemetry limit. This region covers the entire dispersed spectrum. The high energy suppression filter is effectively unusable because of the enhanced background and the need to restrict the active region of the detector. For spectroscopic applications, the quiescent background density is 1.8×10^{-4} cts/s per spectral resolution element. The spectral resolution element is approximately 0.07 Å $\times$0.1 mm in the cross-dispersion direction.

In an effort to reduce the background in post-processing on the ground, we are currently developing an event filtering algorithm which selects events on the basis of pulse height that will preferentially screen out a significant fraction of background events while removing only a small fraction of real X-ray events. The quiescent background rate in the HRC-S is currently about 7×10^{-5} cts/s/arcsecond^2, or 0.12 counts per pixel in 100,000 seconds. As shown in Figure 14, however, this rate can be reduced by about 25%, to 0.09 counts per pixel/100 ksec, simply by excluding events for which pulse height = 255 with essentially no loss ($\ll$ 1%) of x-ray events. When used with the LETG, even larger reductions in background rate (up to $\sim$ 80%) are possible by using position-dependent pulse height filtering. Three factors make this possible: the low but useful energy resolution of the HRC-S; the difference in pulse-height distributions of x-ray and particle background events; and the known correspondence of photon energy with detector position for dispersed spectra.

Using the extensive HRC-S laboratory calibration data, combined with analysis of LETGS spectra obtained on-orbit, the CXC LETG Calibration group has developed a model of mean pulse height value versus detector position for 1st-order photons dispersed by the LETG. Pulse height spectra from a large region of the central segment at five X-ray energies are shown in Figure 15. Over this region the gain varies by as much as 50%. The pulse height distribution for monochromatic photons incident upon a small region of the detector is considerably narrower than those shown in the figure, however. The one sigma width is about 0.22 times the mean pulse height value. The pulse height distribution for background events, in contrast, is relatively broad and flat. By excluding events outside of a limited range around the mean pulse height value, the number of background events can be greatly reduced with little or no loss of real X-ray events. Mean pulse height values decrease in proportion to x-ray energy, so that the x-ray peak moves further below the background mean, resulting in more effective filtering at long wavelengths. This is fortunate, since long-wavelength photons are dispersed more widely in the cross-dispersion direction because of the inherent astigmatism of the grating geometry, and so the spectral extraction region includes more background events than at short wavelengths.

Flight data analysis is still proceeding, but preliminary tests of this pulse height filtering tool show typical background reductions of 60% with 2% x-ray loss, 65% with 5% x-ray loss, and 75% with 15% x-ray loss. The effects of different levels of filtering can be seen in Figure 14. Models could also be generated for use with the HETG, and for an arbitrary source position on the HRC-S. Interested readers are referred to the LETGS Observer Information web page

`http://asc.harvard.edu/cal/Links/Letg/User/`

for more detailed and current information. It is expected that this filtering tool will be ready for public use in March 2000, and that a conservative application of it (i.e., with no more than a 2% x-ray loss) will become part of the standard data processing pipeline. Observers will also be able to tailor the filtering level to their particular needs if more than the standard filtering is required. This filtering will be discussed in more detail in a future publication (Wargelin *et al.*, 2000).

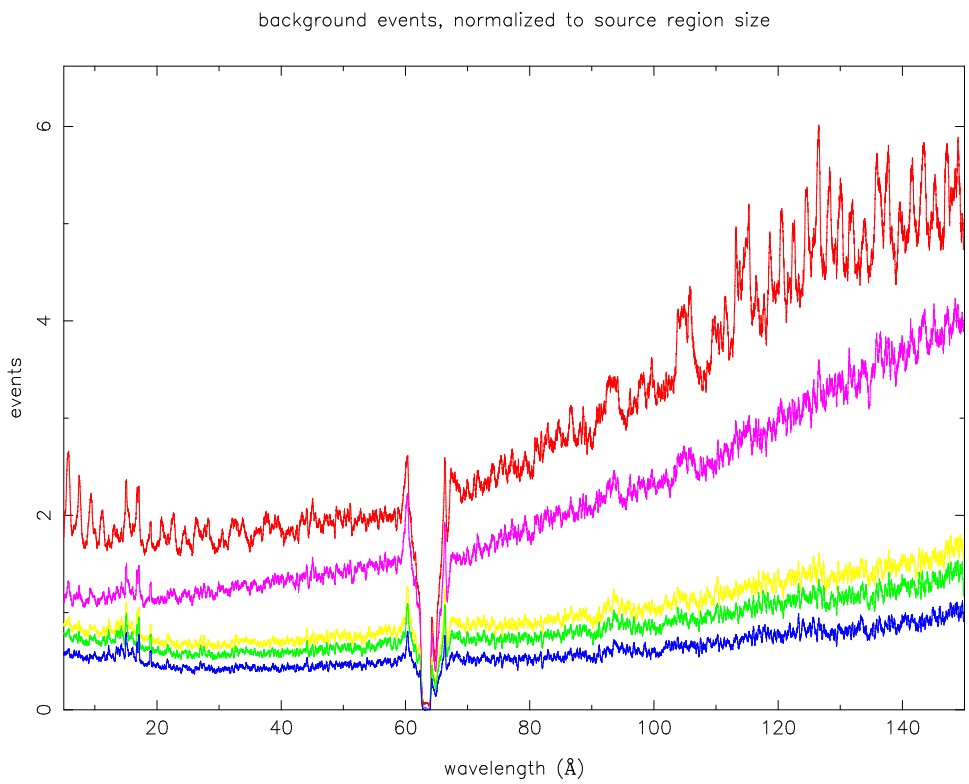

Figure 14: The LETG+HRC-S background spectrum from an observation of Capella filtered by pulse height to different levels of X-ray loss (see text). The curves from the top down correspond to: no filtering; pulse height = 255 events removed with 0% X-ray event loss; filtering with 2% X-ray loss; 5% X-ray loss; and 15% X-ray loss. The units of the y axis are average number of events/bin with a bin size of 6.429 μm, one HRC-S pixel. The X-ray spectral exraction region widens at longer wavelengths. but the background region is much wider to improve statistics. The histograms plotted in this figure are normalized to the source extraction width. The exposure time was 85 ks. The large dip in the data at 62Å is the gap between the segments.

6 UV SENSITIVITY

The sensitivity of the High Resolution Imager (HRI) on ROSAT to ultraviolet radiation was considerably higher than prelaunch estimates (Zombeck *et al.* 1997). because of the higher than predicted UV transmission of the HRI's aluminized Lexan UV/Ion shield. This sensitivity was demonstrated early in the ROSAT mission with the detection of the 0 magnitude star Vega (alpha Lyr; A0V; U=0.02, B= 0.03, V= 0.03; alpha(2000) = 18h 36m 56.2s , dec(2000) = +38 deg. 47' 01") by the HRI at a rate much higher than expected. During the design stage of the HRC-S, we developed a more effective UV/Ion shield by replacing the Lexan substrate with polyimide. By using polyimide, we were able to make a shield that had high transmission to X-rays whilst adequately reducing the transmission to UV and visible light. Because the HRC-S is the readout for the dispersive LETG, it is not necessary to completely block the UV and visible light (see the companion paper on the HRC-I) but only to reduce it sufficiently to prevent the 0 order or "interlopers" (field stars) from saturating telemetry. An observation of Vega imaged at the 0 order position (without the LETG) of the HRC-S to verify the UV and visible response yielded a count rate of 0.2 ct s-1. The predicted count rate calculated by multiplying Vega's spectrum with the HRC-S effective area in the UV and visible spectral bands (see Figure 16) is 1 ct s-1. We are planning observations of additional stellar sources but are confident that the shield exceeds the design goal.

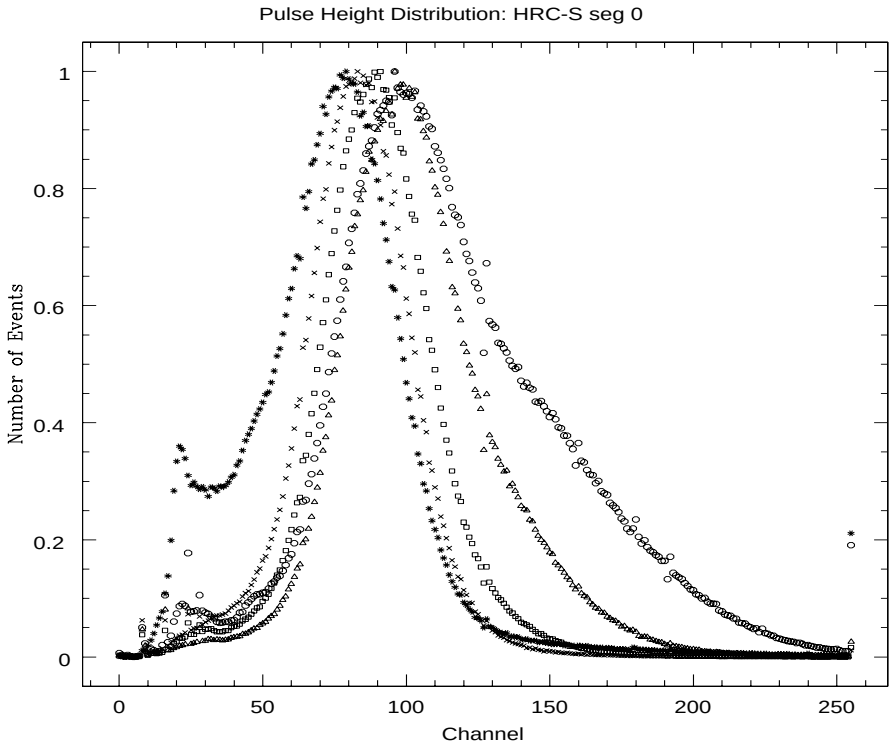

Figure 15: Pulse height distributions of the center segment of the HRC-S at five energies: 183 eV (asterisks), 277 eV (Xs), 525 eV (squares), 1487 eV (triangles), and 6404 eV (circles).

7 POINT SPREAD FUNCTION AND IMAGING PERFORMANCE

The HRC-S is optimized as the readout for the LETG, but the imaging performance of the detector is identical to the HRC-I. Figure 17 contains a plot of the encircled energy of the HRC-S/HRMA as a function of radius for an observation of LMC X-1. Two curves of the pre-launch predicted imaging performance of the HRC-S/HRMA combination are shown for comparison. The measured performance is considerably better than the prediction because the simulations assumed that the aspect solution would be no better than 0.5" (FWHM). In practice the aspect solution is typically better than 0.4". For the LMC X-1 observation, 50% of the counts are contained within a 0.7 arcsecond diameter region, and 90% within a 1.8 arcsecond diameter region.

The HRC-I detector suffers from a 'ghost' image in which a small fraction of the events in every observation are misplaced by about 11 arcseconds along one of the detector axes and is caused by amplifier saturation. At present, there is no evidence of a similar effect in the HRC-S. The 'ghost' accounts for only 2% of the total events from a point source in the HRC-I. If it is present in the HRC-S, it must be several orders of magnitude weaker than in the HRC-I and is therefore of negligible effect for almost all observations. There is no evidence of the 'ghost' in the zeroth order image of HZ 43 which contains several hundred thousand events. We are currently developing an event screening algorithm, called the hyperbolic locus test, to reduce background in the HRC-S, in addtion to the pulse height filtering described above. This test was originally developed for the HRC-I to improve image performance and remove the 'ghost', but it also filters out a significant fraction of the particle background, which is the dominate component of the total instrument background (Murray *et al.* 2000, Kenter *et al.* 2000). We plan to reduce the HRC-S background to the lowest possible level through a combination of filtering on event pulse height and application of the hyperbolic locus test. A more complete discussion of the

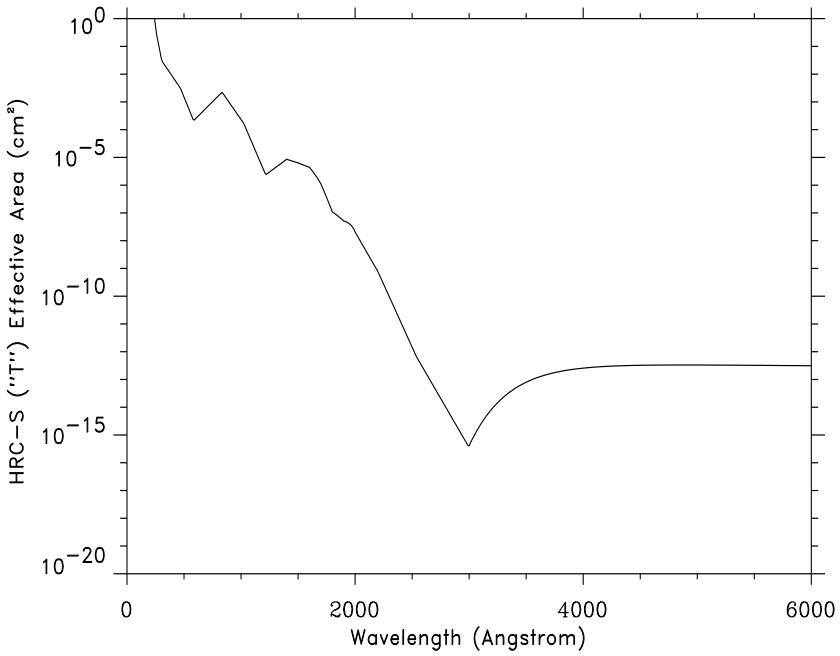

Figure 16: UV sensitivity of the central segment of the HRC-S as a function of wavelength.

'ghost' image and event filtering is contained in Murray *et al.* 2000 and Kenter *et al.* 2000.

8 SUMMARY AND FUTURE WORK

We have presented preliminary results of the on-orbit calibration of the HRC-S including detector quantum efficiency, background, and imaging performance and compared with pre-flight estimates. We have also described in detail the pre-flight QE calibration. Except for the increased background, the instrument is performing as expected. Preliminary analysis of the QE verification data indicates that the HRC-S QE is within ~10% of our pre-launch estimates above 0.5 keV, and we have used the observations of HZ 43 and Sirius B to calibrate the HRC-S/LETG efficiency below 200 eV. We are optimistic that much of the enhanced background will be reduced by careful filtering of events on pulse height value and application of the hyperbolic locus test.

9 ACKNOWLEDGEMENTS

We would like to thank Dr. Martin Barstow of Leicester University for providing model spectra of Sirius B and HZ43. We are grateful for the support of Jack Gomes, Everett Johnston, John Boczenowski, John Polizotti, Richard Goddard, Frank DeFreze, Joseph D'Arco, Desi Hamvaz, and Frank Rivera. This work has been supported by NASA contracts NAS8-38248 and NAS8-39073.

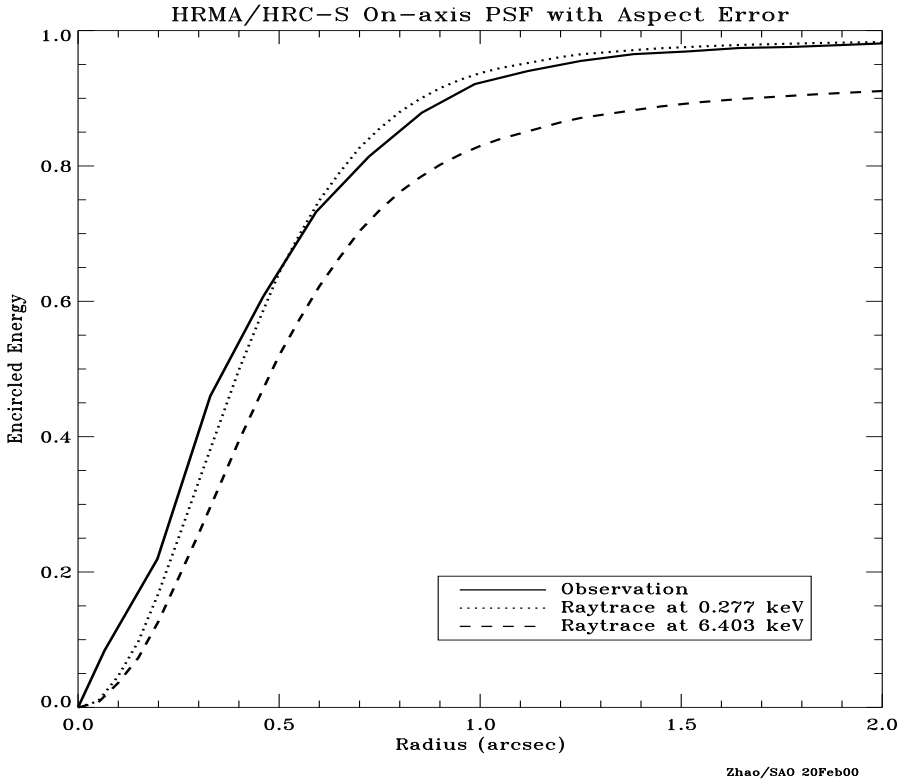

Figure 17: Fractional encircled energy of the HRC-S/HRMA combination. The solid curve is the in-flight observation of LMC X-1, the two dashed curves are raytrace simulations of the HRMA with contributions for the finite resolution of the HRC and the aspect solution applied.

10 REFERENCES

1. M. C. Weisskopf, S. L. O'Dell, R. F. Elsner, and L. P. Van Speybroeck, *X-ray and Extreme Ultraviolet Optics*, R. B. Hoover and A. B. C. Walker, Jr., eds., Proc. SPIE 2515, 1995.

2. S. L. O'Dell and M. C. Weisskopf, *X-Ray Optics, Instruments, and Missions*, R. B. Hoover and A. B. C. Walker II, eds., Proc. SPIE, 1998.

3. A. C. Brinkman, J. J. van Rooijen, J. A. M. Bleeker, J. H. Dijkstra, J. Heise, P. A. J. de Korte, R. Mewe, and F. Paerels, *Astro. Lett. and Commun.*, 26, 1987.

4. C. R. Canizares *et al.*, *Astro. Lett. and Commun.*, 26, 1987.

5. S. S. Murray *et al.*, *Astro. Lett. and Commun.*, 26, 1987.

6. J. A. Nousek *et al.*, *Astro. Lett. and Commun.*, 26, 1987.

7. R. P. Kraft *et al.*, *EUV, X-Ray, and Gamma-Ray Instrumentation for Astronomy VIII*, O. H. W. Siegmund and M. A. Gummin, eds., Proc. SPIE 3114, 1997.

8. G. R. Meehan, S. S. Murray, M. V. Zombeck, R. P. Kraft, K. Kobayashi, J. H. Chappell, A. T. Kenter, M. Barbera, A. Collura, and S. Serio, *EUV, X-Ray, and Gamma-Ray Instrumentation for Astronomy VIII*, O. H. W. Siegmund and M. A. Gummin, eds., Proc. SPIE 3114, 1997.

9. S. S. Murray *et al.*, *EUV, X-Ray, and Gamma-Ray Instrumentation in Astronomy, VIII*, O. H. W. Siegmund and M. A. Gummin, eds., Proc. SPIE, 3114, 1997.

10. A. T. Kenter *et al.*, *EUV, X-Ray, and Gamma-Ray Instrumentation in Astronomy, VIII*, O. H. W. Siegmund and M. A. Gummin, eds., Proc. SPIE, 3114, 1997.

11. D. Patnaude *et al.*, *X-ray Optics, Instruments, and Missions*, R. B. Hoover and A. B. C. Walker II, eds., Proc. SPIE 3444, 1998.

12. R. P. Kraft *et al.*, *EUV, X-Ray, and Gamma-Ray Instrumentation for Astronomy VII*, O. H. W. Siegmund and M. A. Gummin, eds., Proc. SPIE 2808, 1996.

13. P. Zhao *et al.*, *X-Ray Optics, Instruments, and Missions*, R. B. Hoover, and A. B. C. Walker II, eds., Proc. SPIE 3444, 1998.

14. J. M. Auerhammer *et al.*, *X-Ray Optics, Instruments, and Missions*, R. B. Hoover, and A. B. C. Walker II, eds., Proc. SPIE 3444, 1998.

15. B. L. Henke, E. M. Gullikson, and J. C. Davis, Atom. Data and Nucl. Data Tables, 54, 1993.

16. J. H. Scofield, Atom. Data and Nucl. Data Tables, 14, 1974.

17. M. Juda, SAO Internal Memo, 1997.

18. B. L. Henke, J. P. Knauer, and K. Premaratne, Journ. of Appl. Phys., 52, 1981.

19. A. Owens, S. C. Bayliss, P. J. Durham, S. J. Gurman, and G. W. Fraser, Ap. J., 468, 1996.

20. A. T. Kenter, SAO Internal Memo, 1998.

21. J. J. Kolodziejczak, R. A. Austin, R. F. Elsner, M. K. Joy, M. Sulkanen, E. M. Kellogg, and B. J. Wargelin, X-Ray and Extreme Ultraviolet Optics R. B. Hoover and A. B. Walker, eds., Proc SPIE 2515, 1995.

22. R. P. Kraft, A. T. Kenter, S. S. Murray, J. Gomes, and E. Johnston, *EUV, X-Ray, and Gamma-Ray Instrumentation for Astronomy X*, O. H. W. Siegmund and K. A. Flanagan, eds., Proc. SPIE 3765, 1999.

23. R. M. Rideout *et al.*, *EUV, X-Ray, and Gamma-Ray Instrumentation in Astronomy IX*, O. H. W. Siegmund and M. A. Gummin, eds., Proc. SPIE 3445, 1998.

24. A. C. Brinkman *et al.*, Ap. J., 530, 2000.

25. S. S. Murray *et al.*, *X-ray Optics, Instruments, and Missions*, J. Trumper and B. Aschenbach, eds., Proc. SPIE 4012, 2000.

26. A. T. Kenter *et al.*, *X-ray Optics, Instruments, and Missions*, J. Trumper and B. Aschenbach, eds., Proc. SPIE 4012, 2000.

27. A. C. Brinkman *et al.*, *X-ray Optics, Instruments, and Missions*, J. Trumper and B. Aschenbach, eds., Proc. SPIE 4012, 2000.

28. M. A. Barstow, J. B. Holberg, and D. Koester, MNRAS, 274, 1995.

29. F. B. S. Paerels, J. A. M. Bleeker, A. C. Brinkman, and J. Heise, Ap. J., 329, 1988.

30. S. E. Pearce, J. E. Lees, J. F. Pearson, G. W. Fraser, A. N. Brunton, K. A. Flanagan, A. T. Kenter, M. Barbera, V. Dhanak, A. Robinson, and D. Teehan, *EUV, X-Ray, and Gamma-Ray Instrumentation in Astronomy VI*, O. H. W. Siegmund and J. V. Vallerga, eds., Proc. SPIE 2518, 1995.

31. M. V. Zombeck, M. Barbera, A. Collura, and S. S. Murray, Ap. J. Lett., 487, 1997.

32. B. Wargelin *et al.*, *in preparation*, 2000.